Integrated Photonic Spectroscopy

Applying the Digital Fourier-Transform Spectrometer

By:
Gillian K. Micale
B.S., Engineering Physics
Stanford University, 2018

Submitted to the MIT Department of Materials Science and Engineering
in Partial Fulfillment of the Requirements for the Degree
of

Master of Science in Materials Science and Engineering

at the
MASSACHUSETTS INSTITUTE OF TECHNOLOGY

May 2022

©Massachusetts Institute of Technology. All rights reserved.

Signature of Author .....

Department of Materials Science and Engineering
May 4, 2022

Certified by .....

Juejun Hu
Associate Professor
Thesis Supervisor

Accepted by .....

Frances M. Ross
Chair, Departmental Committee on Graduate Studies

THIS PAGE INTENTIONALLY LEFT BLANK

Integrated Photonic Spectroscopy

Applying the Digital Fourier-Transform Spectrometer

by

Gillian K. Micale

Submitted to the Department of Materials Science and Engineering
on May 11, 2022, in partial fulfillment of the requirements
for the degree of
Master of Science in Materials Science and Engineering

Abstract

The digital Fourier-Transform (dFT) spectrometer is a promising on-chip spectrometer architecture that offers exponential scaling for resolution with a compact device footprint. A package of scripted modules employs object-oriented programming to automate creating the mask layout and streamline the dFT design process. Moving towards longer infrared wavelengths with broadband devices expand the sensing capabilities by accessing stronger chemical absorption signatures associated with the fingerprint regime. The second generation of dFT devices realizes two high-resolution, 1024-channel spectrometers. The first device operates around 1550 nm and fully utilizes foundry standard components and processes. The second device achieves half-octave operation between 1620 - 1750 nm with the use of custom broadband adiabatic couplers. The next set of designs push beyond the telecom range, combining two dFT devices on a single chip for 1.2 - 2.4 µm operation. Ultra-broadband single-mode waveguides and custom adiabatic couplers were designed for each device on this chip. All four of the discussed designs use the SOI material platform and are compatible standard foundry processes.

Thesis supervisor: Juejun Hu
Title: Associate Professor of Materials Science and Engineering

THIS PAGE INTENTIONALLY LEFT BLANK

Contents

1 Introduction **6**
1.1 Motivation 6
1.2 Background 8

2 Design Approach **11**
2.1 Deign Concepts 11
2.2 Programmatic Methodology 12

3 Devices **16**
3.1 High-resolution and Broadband Designs 16
3.2 Ultra-broadband dFT System 18

4 Conclusion **22**

5 References **23**

1 Introduction

1.1 Motivation

Spectroscopic sensing facilitates the detection of chemical compounds using absorption signatures. Applications including biochemical sensing, environmental sensing, toxic gas monitoring, industrial process control, and even exotic applications like astrophysics present impactful opportunities to employ spectroscopic sensing in many facets of society.[1–4] The phonon vibrational states of molecules create unique, wavelength-dependent absorption signatures. Many key chemical resonant frequencies exist in the so-called "fingerprint region" of the mid-infrared (MIR) spectral region, while harmonics of these frequencies and certain functional group resonances may be found at smaller IR wavelengths (Fig. 1).

Absorption spectroscopy is conducted by exposing a sample with light and analyzing the resulting spectral information. The wavelengths of the absorption peaks in the collected spectrum relate directly to the chemical species' structural resonances and are used to identify the species present. The magnitudes of the absorption peaks are used to quantify the concentrations of each species, as the absorption scales linearly with the concentration.[5]

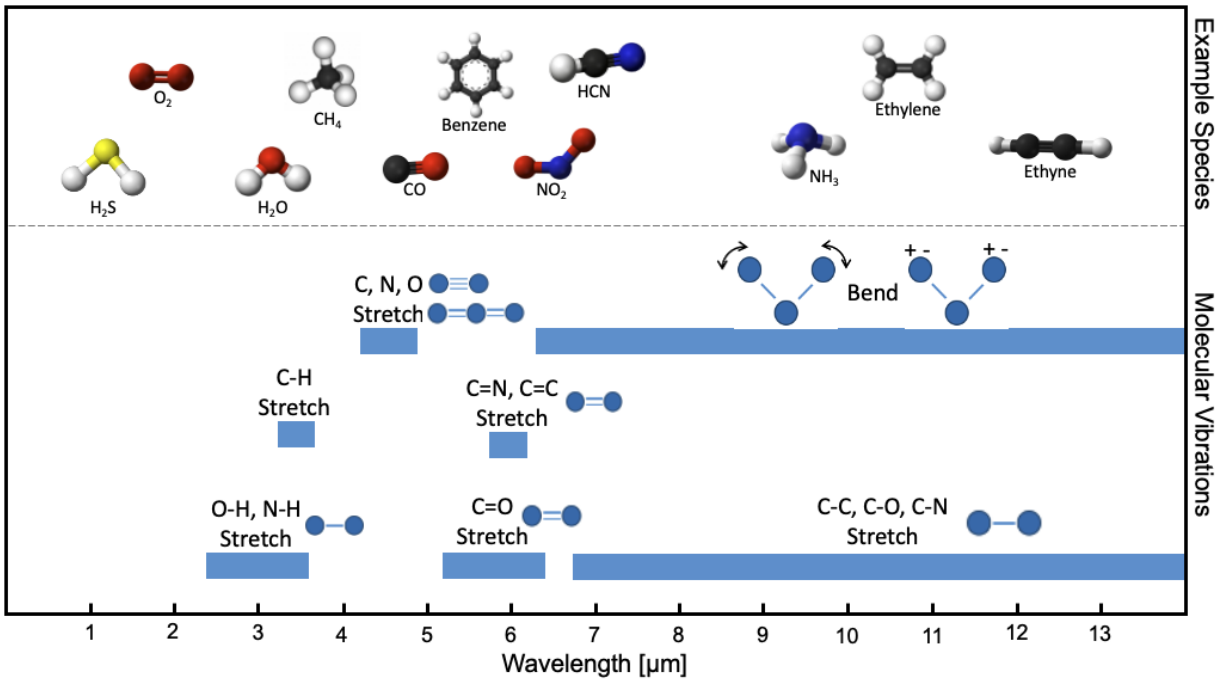

Figure 1: Diagram of chemical absorption signatures. The lower portion shows the resonance of different functional groups and the corresponding absorption wavelength ranges.[6] Above, example species are depicted associated with the approximate wavelength of their phonon resonances.[7]

Spectral information can be collected either using dispersive spectroscopy or with Fourier-transform spectroscopy (FTS). The former splits light by wavelength spatially using a dispersive element and collects each portion of the light using an array of detectors. Whereas FTS uses a dynamic system to create a time-dependent electric field distribution which is then collected at a single detector. Since the light is concentrated at one detector, the latter assumes the multiplex advantage which, compared to dispersive spectroscopy, enhances the signal-to-noise ratio (SNR) by a factor of $\sqrt{N}/2$ with N being the number of spectral channels of the spectrometer.[8,9]

The instrument used in FTS is functionally an interferometer. As shown in Figure 2, the light beam is split into two paths. One path has a fixed length, while the other is varied using a moving mirror. Based on the optical path difference (OPD) between the two paths, the recombined light will exhibit constructive or destructive interference. The input spectrum is recreated using the Fourier relation between the wavelength-dependent spectrum and the time-dependent interferogram.[10]

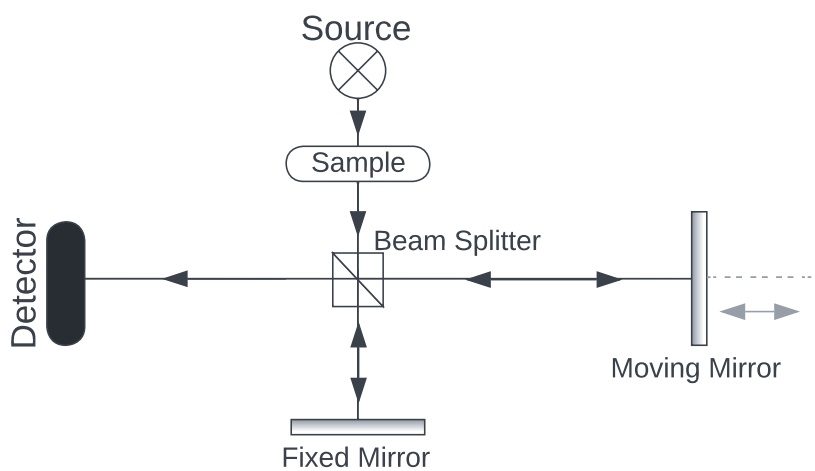

Figure 2: Schematic of the interferometry used in FTIR spectroscopy. Input light is incident on a beam splitter which directs light down two paths. By moving the mirror on one of the path, the path length difference is varied which changes the interference condition of the recombined light at the detector.

Fourier-transform Infrared (FTIR) spectrometers are instruments commonly used for FTS. As discussed previously, the IR is a spectral region of great interest for absorption spectroscopy. FTIRs are bench-top instruments that house free-space optics for the interferometer. FTIR systems are expensive, usually costing tens of thousands of dollars, and require frequent calibrations to keep the optical components in alignment. Using microphotonic integration is an enticing alternative to traditional spectrometers. Photonic integrated circuit (PIC) technology would enable inexpensive, durable, and reliable solid-state on-chip spectrometers. Benefiting from established high-volume manufacturing processes

for semiconductor devices, the unit cost for a spectrometer would be a fraction of what is currently paid for bench-top instruments. The monolithic nature of integrated circuits eliminated the need for frequent calibration, and the size reduction supports the eventual use of portable spectrometers for field-deployed applications.

1.2 Background

On-Chip Spectrometers

While on-chip spectrometers would have great size, weight, power, and cost advantages over traditional instruments, miniaturizing a spectrometer while maintaining performance is its own challenge. Resolution scales inversely with the maximum path length which is significantly limited for a chip scale device. Most research efforts to make an on-chip FTS follow one of two approaches: (1) creating a tunable Mach-Zehnder Interferometer (MZI) using direct index modulation to control the effective path lengths of the two waveguides,[11–14] and (2) implementing the spatial heterodyne spectroscopy principle with arrays of discrete MZIs of increasing OPD.[15–19] The first approach is limited by the fact that direct refractive index modulation has a relatively small impact on the effective optical path length, so even with long waveguides and a large chip footprint the spectral resolution is limited to tens of cm^{-1} in wavenumber. Devices following the second approach also require large footprints for waveguide length and are not practical for high spectral channel counts, both aspects limiting the potential resolution of these spectrometer. To achieve resolution that rivals a macro-scale instrument in an on-chip spectrometer, different approach is necessary for modulating the optical path lengths.

Previous Work

In previous work, this group introduced a new on-chip spectrometer architecture with great potential for scalability.[20–22] This design utilizes a two sets of cascading optical switches to make a tunable interferometer with quantized optical path differences (OPDs). The digitally addressed switches actuate unique permutations of waveguide paths to create a set of discrete optical path length combinations in the two arms of the interferometer. With the switches in the base state, the OPD between the two arms is zero. Then as switches are triggered, the OPD grows by factors of $n_g \cdot L$ times powers of two, where n_g represents the group index of the waveguide. For j switches, the maximum OPD is $(2^j - 1) \cdot n_g \cdot \Delta L$. Following the Rayleigh criterion, this yields a spectral resolution given by:

$$\delta\lambda = \frac{\lambda^2}{(2^j - 1) \cdot n_g \Delta L} \approx \frac{1}{2^j} \cdot \frac{\lambda^2}{n_g \Delta L} \tag{1}$$

where λ is the center wavelength. The spectral channel count is defined by the number of unique OPDs: $N = 2^j$. As such, both the resolution and spectral channel count scale

exponentially with the number of switches while maintaining a small device footprint.

Before a dFT device can be used as a spectrometer, it must be characterized to determine the Fourier relation between the input spectra and the collected interferograms. This relationship is given by the linear equation $\mathbf{y} = \mathbf{A}\mathbf{x}$, where $\mathbf{x}$ represents any arbitrary polychromatic input, $\mathbf{y}$ is the measured interferogram, and $\mathbf{A}$ is the device-specific characterization matrix.

The dimensions of the $m \times n$ matrix $\mathbf{A}$ depend on m, the number of spectral channels, and n the number of wavelength points in the input spectra. For the 64-channel prototype, $m = 64$ and $n = 801$, making the linear equation under-constrained, so regularization is required to find a unique solution. An "Elastic-D_1" regression method was used to solve for A while accounting for the sparsity, magnitude, and smoothness of the recorded spectra using the following condition:

$$\min_{\mathrm{x},\mathrm{x}>0}\{||\mathbf{y} - \mathbf{A}\mathbf{x}||_2^2 + \alpha_1||\mathbf{x}||_1 + \alpha_2||\mathbf{x}||_2^2 + \alpha_3||\mathbf{D_1}\mathbf{x}||_2^2\} \tag{2}$$

Here α_1 and α_2 assign weights to the L_1- and L_2-norms of $\mathbf{x}$ and α_3 weighs the L_2-norm of the first derivative of $\mathbf{x}$, specified by $\mathbf{D_1}$.

This digital Fourier-Transform (dFT) architecture was experimentally demonstrated with a 64-channel spectrometer. The device was fabricated at a professional Si photonics foundry, utilizing standard processes and components. This C-band spectrometer had 6 total switches, giving it a spectral resolution of around 0.4 nm. The optical switches were comprised of custom thermo-optic (TO) modulators with a phase shifting efficiency of 33 mW/π . MMIs from the foundry process design kit were used for the coupling elements. Light was coupled on to the chip with grating couplers, and the output was collected by Ge photodetectors.

In use, it was determined that this device could resolve two laser lines with a separation of $\delta\lambda = 0.2$ nm. This outperforms the Rayleigh Criteria estimate as a result of the Elastic-D1 regression method. Further testing verified the device's ability to reconstruct arbitrary input spectra and fine spectral features. This validated the dFT architecture which could then be scaled to have more switches and finer resolution.

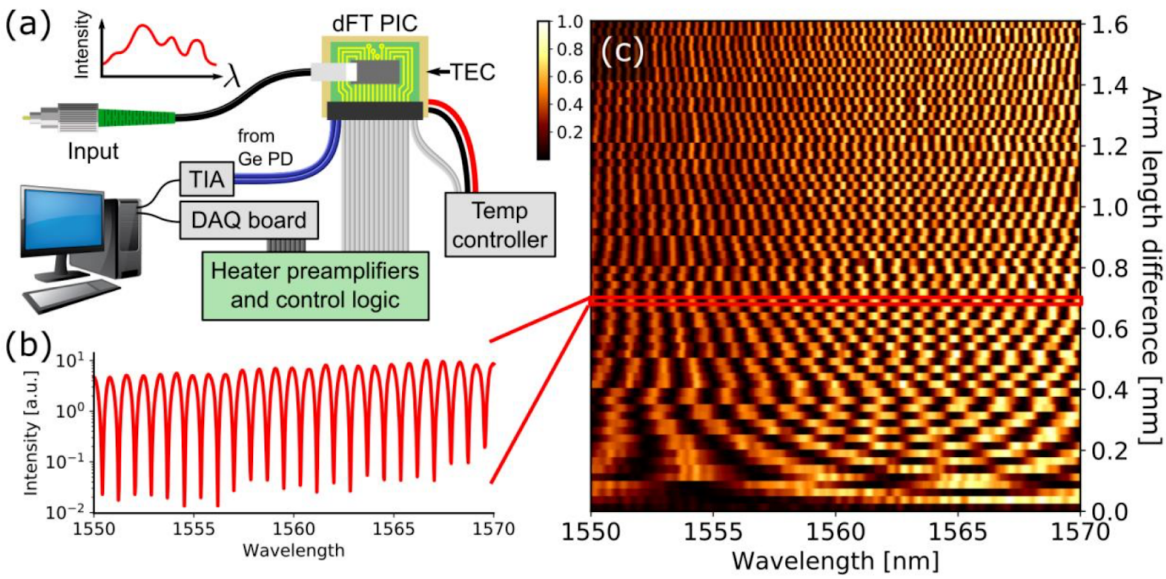

Figure 3: (a) Schematic of the experimental setup for characterizing and testing dFT devices. (b) An example transmission spectrum measured by the dFT device corresponding to an optical path difference of 0.7 mm. (c) Transmission spectra are compiled into a spectral basis from which the input spectrum may be reconstructed. Each row represents a unique device state ($m = 64$ total) and contains intensity measurements for all n wavelength samples. Reprinted from [18].

2 Design Approach

2.1 Deign Concepts

To rival bench-top spectrometers a dFT device must have sub 1 cm^{-1} resolution across a considerable spectral range. Since the resolution is related to the maximum OPD, as shown with the Rayleigh Criteria in Equation 1, the resolvable distance between features is determined by the spectral channel count and the relative path length difference between optical states, which is set by the scaling factor ΔL. Increasing the number of switches exponentially improves the resolution. Additionally, optimizing L to increase the maximum OPD while balancing device footprint and overall propagation loss further guarantees a high spectral resolution.

Another design consideration is the device's bandwidth of operation. The spectral window is decided based on the target species detection. As previously mentioned, absorption signatures in the near and mid IR allow for highly accurate detection and differentiation of chemical species. A larger bandwidth improves the functionality of the spectrometer by increasing the versatility of the detection of chemical species. But since the bandwidth of the device is limited by the bandwidth of the components, broadband design sacrifices the convenience of using proven, standard, telecom components available through professional foundries. The original dFT device used grating couplers for on-chip coupling and MMIs for power coupling, both of which limit the bandwidth to a few tens of nanometers. Substituting edge couplers for fiber-chip coupling and using broadband power couplers are two ways to improve the bandwidth.

Beyond improving resolution and bandwidth, an additional change that can be made to the original dFT design is adding the features of arm balancing and fringe alignment, as noted in the schematic in Figure 4. By adding and additional pair of phase modulators to the end of each major arm, light can be directed to either the arm's taps or to the combiner for the total device output. Crucially, this feature prevents 3 dB of loss the original device incurred since the output light was always split between the taps and the output. The other added feature, fringe alignment, is achieved with the addition of a phase modulator preceding the repeating stages on each major arm. These modulators allow the phase of the light in each arm to be continuously adjusted, which can be used to shift the resonant peaks of the output and effectively filter out excitation lines from laser sources.

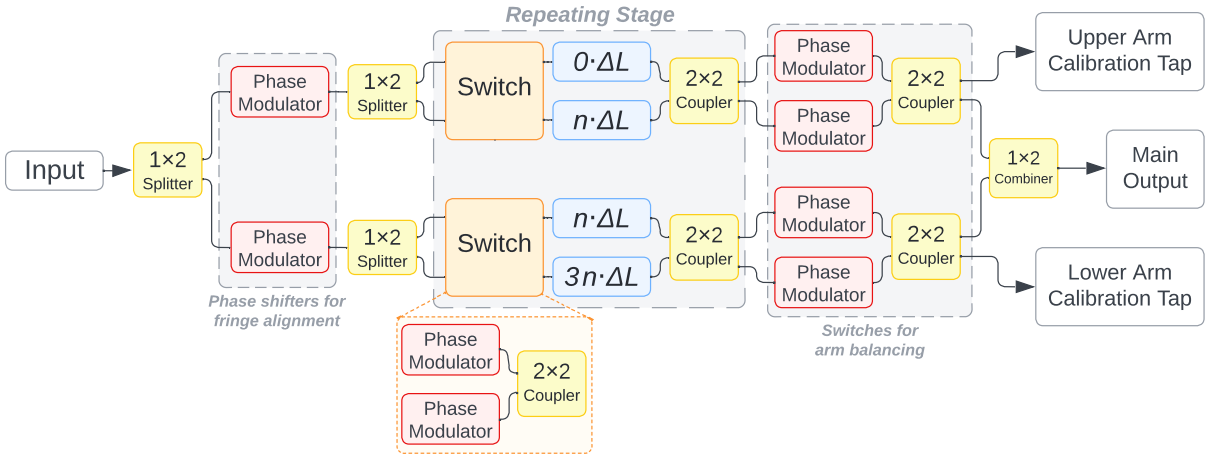

Figure 4: Schematic of the updated dFT spectrometer architecture. The new design includes phase modulators for fringe alignment and switches at the end of each arm for arm balancing. The repeating stage consists of an optical switch, a pair of waveguides, and a 2×2 power coupler. The delay lengths of each waveguide are multiples of ΔL and follow the pattern shown above where $n = 1, 2, 3, ...$ corresponding to the number of the stage.

2.2 Programmatic Methodology

The creation of a PIC device starts with a mask design which assembles the constituent photonic components into a visual representation of the device and translates the design into fabrication layers and processes. This design can be made manually with the pick-a-place method using software like *KLayout*. As the design becomes more complex, this method becomes arduous and versioning is time consuming as minor edits can mean redoing the placement of large portions of the layout.

Tools like the IPKISS Photonics Design Platform address that issue. Using object-oriented programming, IPKISS synthesizes the different steps of the PIC design process and streamlines the PIC design process by integrating component and circuit level simulation and design with foundry components and design rule checks into a single platform. In a scripting environment, the photonics circuit may be constructed out of components and waveguides represented by coded objects and stitched together with *place* and *join* functions. Implementing a programmatic approach to mask design decreases the revision time and improves the adaptability of the design.

The first paradigm of programmatic design would be to specify the set of parameters which define the device and have the mask design generated automatically. For a dFT device, the design comes down to five core parameters: the number of stages, power splitter, power coupler, phase modulator, and OPL scaling factor (ΔL). As discussed previously, the choices of these parameters are informed by the target bandwidth and resolution performance of the dFT, but the parameters themselves are consistent across all possible de-

signs and are a suitable basis for scripting the programmatic design.

The second paradigm of this programmatic approach is to represent the device architecture in a modular fashion by decomposing the device into its compositional pieces. This adds to the flexibility of the design script and allows the designer to customize aspects of the design without creating a design from scratch. To accomplish this, we must consider the composition of the device and how it may be represented by a hierarchy of objects.

Utilizing the IPKISS platform, a set of Python objects was constructed which may then be assembled into a dFT design, shown by the hierarchy depicted in Figure 5. First, the global variables are defined, including the waveguide template that represents the structure of the waveguide and the bending radius that will be used throughout the device. Then the modules are used to combine switching stages into super-arms which represent the upper and lower branches of the interferometer. These arms are assembled with input and output coupling to create the dFT device.

The modules are created as IPKISS Parametric Cells, or PCells, which are reusable units that use parameters to calculate the details of said unit. The modules inherit the PCell sub-classes that are used to layout the physical circuit and create a circuit model that can be used in simulation. The parameters used by the PCell are a combination of traditional data types like floats and IPKISS Child Cells, other PCells which are themselves used as sub-units for the new PCell. In the dFT module hierarchy, stages are combined into the major arms of the dFT which are then used as Child Cells for the full device. The global parameters apply to all modules and are consistent throughout the device; these are the waveguide template, bending radius, and the power splitter[1] and modulators Child Cells.

For the design of a dFT, first the *Stage* module is used to create instances of the device's switching stages. The input arguments describe the vertical separation of the modulators and all of the information needed to make the two waveguide paths. The arm lengths specify the lengths of each optical path while the rest of the arm parameters specify the shape the waveguide path will take. The type argument is a string which designates which of the four routing types should be used for each path.[2] The direction indicates whether the waveguide extends to the left or to the right. The number of loops is used for the spiral routing functions to adjust the overall length and width of the spiral waveguides. The sub-units of waveguide segments, modulators, and power couplers are placed and joined to construct the stage PCell.

Next, the stages are used as Child Cells in the *SuperArm* module. The module also takes in a Boolean argument representing whether or not fringe alignment modulators are

[1]Using MMIs requires 1×2 and 2×2 power splitter options, but when using adiabatic couplers the power splitter is universal. An alternative version of the dFT script modules accommodates the use of MMIs.

[2]Routing type should be decided based on the most space-efficient option for a given waveguide length. The threshold for using a spiral or double-spiral waveguide path depends on the path length scaling and the sizes of the components used within the stages, so the decision is left to the discretion of the designer.

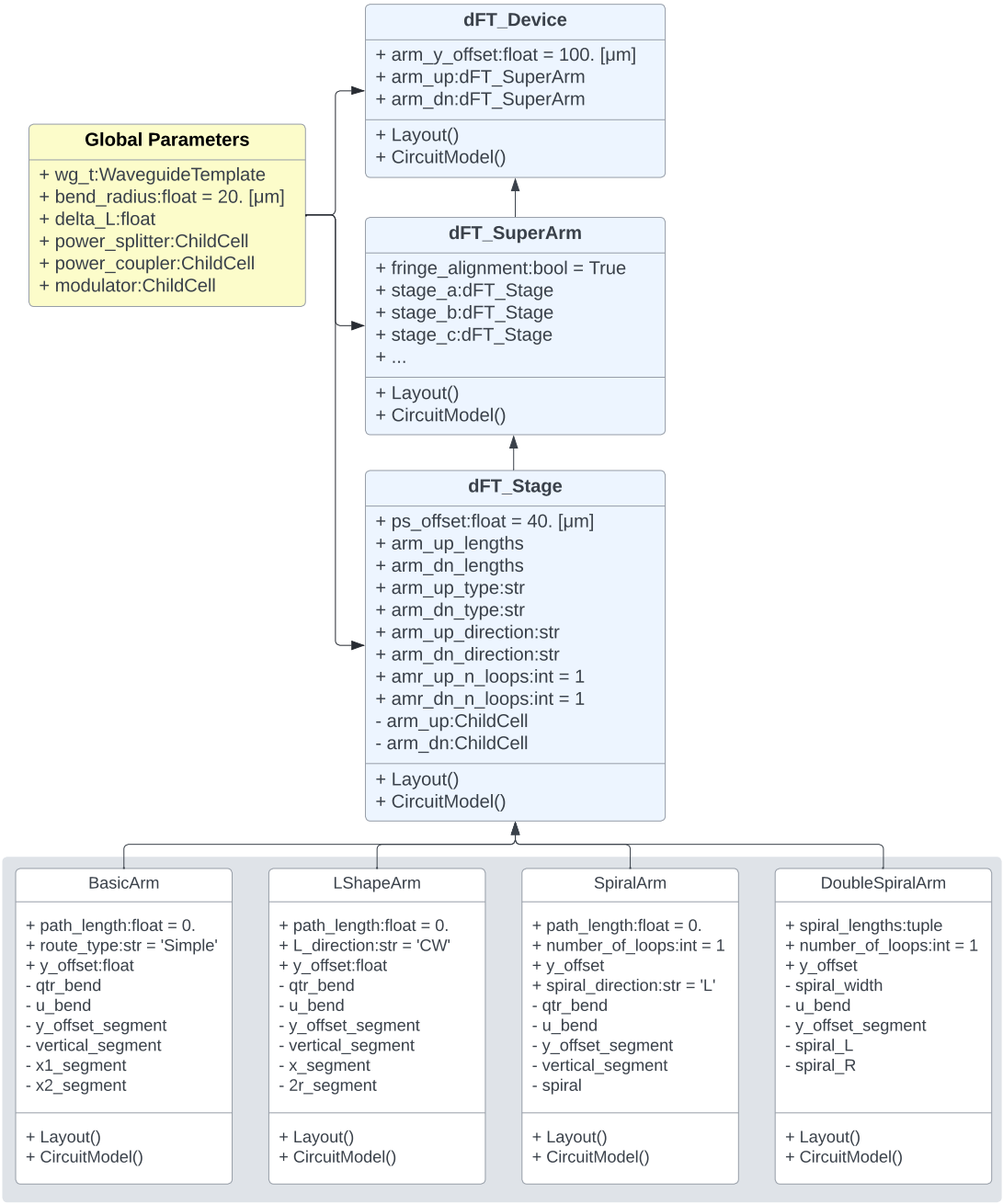

Figure 5: Hierarchy of the modular design structure. First the global parameters are defined. Then the dFT is constructed from stages that form two super arms and are combined into a device. The stage level class uses four routing classes to create the individual stage delay waveguides. These four classes are private to the user and shown here contained in the grey box.

to be included in the dFT design. Variations of this module can be used depending on the number of stages per arm for a given dFT. For a 5-stage device, stages a-e would be created by the designer and used as input parameters for each of the arms.

Finally, the two major arms are combined in the *Device* module. The vertical distance between the two arms is specified to ensure clearance between the different circuit components. Power splitters are placed at either end of each arm to split the light from the chip-coupling input and recombine the light at the output of the device. Adjustments to the Device class can be made to account for different off-chip coupling.

This implementation of a hierarchy of modules simplifies the design process while still allowing for a large degree of customization. Using a programmatic approach, a dFT device may be created simply by specifying a set of global parameters, creating stages with the required arguments, and assembling the stages into a device using the predefined objects.

3 Devices

The dFT prototype established the architecture as a promising, scalable on-chip spectroscopy solution. Building on this previous work, several new designs have been created with the aim to prove the functionality for of dFT spectrometers at higher resolutions, larger bandwidths, and longer wavelengths. The resolution is improved by implementing addition switching stages to increase the spectral channel count. Increasing the bandwidth requires the use of different components, namely for on-chip coupling and power splitting. The further the operation range diverges from telecom frequencies, the more customization is required for a dFT design.

3.1 High-resolution and Broadband Designs

The second generation of dFT designs realized improvements to resolution and bandwidth. Two different dFT design were included on a chip that was fabricated at the AMF foundry SOI multi-project wafer (MPW) run.

The first design on this chip improves the resolution by increasing the spectral channel count. Having 5 repeating stages and 10 total switches, this high resolution dFT has a spectral channel count of 1024. While the 64-channel dFT prototype achieved a resolution of 0.2 nm, this new design has a resolution of 20 to 40 pm. This design leverages components available through AMF's process design kit (PDK) library to ensure the greatest possible fabrication reliability. C-band MMIs and thermos-optic phase modulators are used throughout the device. Each of the major arms has a 1% optical tap to siphon off a small portion of light for calibrating the switching voltages for the first three stages. All light outputs are collected using on-chip Ge photodetectors, also available through the PDK.

The second device expands past the resolution improvements to realize a broadband, high-resolution dFT design. The first bandwidth limiting issue that was addressed were the grating couplers used for on-chip coupling in the prototype design, and the second was the MMIs used for power coupling in both the prototype and the high-resolution designs. Around the C-band, grating couplers and MMIs limit the operation range to a few tens of nanometers, so broadband substitutions must be used for these components in the new design. To replace the grating couplers, edge coupling was used to coupler light onto the chip. The edge couplers followed a reverse taper design to expand the waveguide mode at the chip edge to more closely match the fiber mode and limit the loss arising from mode size mismatch.

To avoid the bandwidth limitation of MMIs, adiabatic couplers were designed that could be used for both 1×2 and 2×2 power splitting. In an adiabatic coupler, the fundamental mode of a single waveguide is adiabatically converted into either the even or odd mode of two waveguides of the same width separated by some distance.[23–25] This is accomplished by gradually tapering two parallel waveguides, one initially larger and the other

initially smaller than the waveguides at the end of the taper region, as shown in Figure 6. In this situation, the slow transition of the two waveguides ensures that only one fundamental mode is ever excited. When light is injected into the coupler from either of the input ports, 3-dB power splitting occurs yielding equal power in the two output waveguides. In the reverse configuration where light is injected from the symmetric side, the phase difference dictates the output of the light: a phase difference of π directs the light to the smaller waveguide output while a phase difference of zero directs the light to the larger waveguide output. Based on this condition, the adiabatic coupler can be paired with modulators to control the phase of the light to create an optical switch with binary positions. For this dFT design, custom doped-silicon thermo-optic modulators were used to guarantee a π-phase shift over the entire operation range.

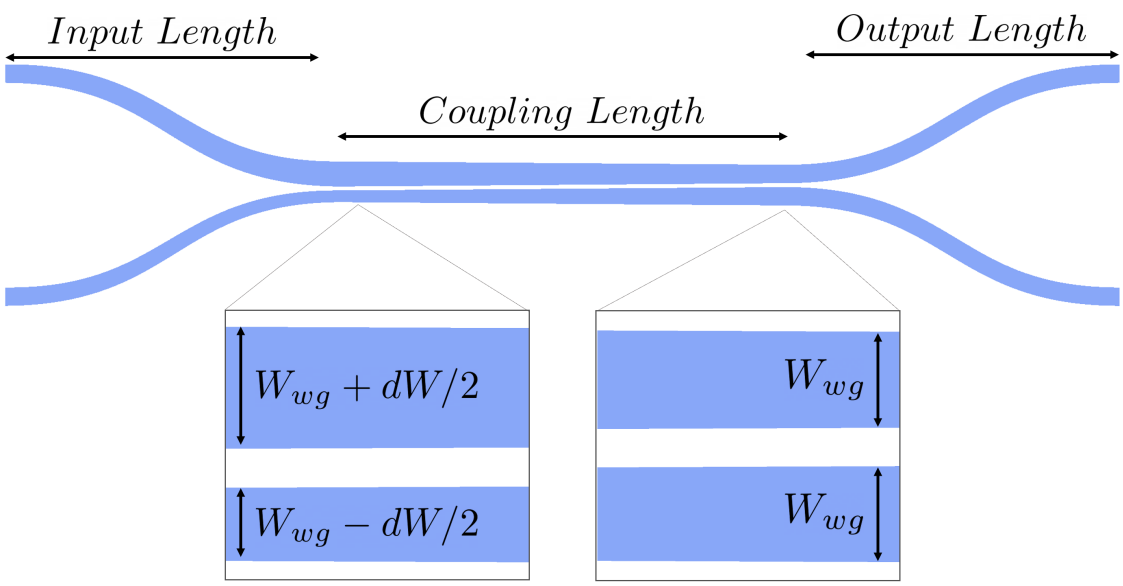

Figure 6: Adiabatic coupler structure with views of symmetric and asymmetric ends of the tapered coupling section.

The mask design for each dFT was created with the fore-mentioned modular design script. This script was developed first during the design of the high-resolution dFT. Then the input parameters were changed to use the relevant components and the broadband design was created. Both dFT devices used a scaling factor of $\Delta L = 20$ µm in order to balance resolution, propagation loss, and device footprint.

After the chips were fabricated at AMF in 2021, they were sent to a company named PHIX for packaging with electronic and optical connections[3]. The chips were mounted on a custom PCB that wire-bonded to the chip's metal contacts. A thermos-electric cooler was mounted underneath the chip to provide thermal stabilization during dFT operation.

[3]PHIX is partnered with a European consortia the aim to connect academia and industry to streamline and standardize photonic assembly packaging

A fiber array with an attached glass interposer was aligned and affixed to the side of the chip of on-chip edge-coupling. The finished, packaged chips were received at the end of 2021 and are currently being characterized (Fig. 7).

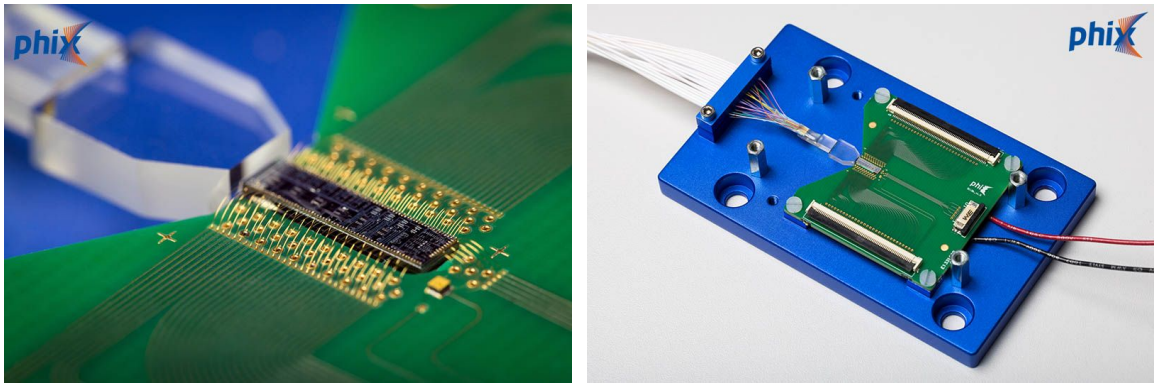

(a) (b)

Figure 7: Packaged chip with High Resolution dFT and Broadband dFT devices: (a) Close up view of chip, electrical connections, and glass inter-poser. (b) Full view of the chip packaging with mounting plate, attached fibers, and sub-mounted TEC.

3.2 Ultra-broadband dFT System

The usefulness of a dFT spectrometer depends on the accuracy of chemical species detection and the breadth of species that may be detected. The importance of versatile functionality motivates the design of broadband dFT spectrometers. For this an evolution of integrated photonic components is necessary. Up to the transparency limit of silicon oxide around 4 µm, SOI remains a useful materials platform,[26,27] and by adjusting component design extremely broadband spectrometers may be created using this platform.

The next demonstration of the dFT architecture pushes the bounds of broadband design and presents two dFT devices on a single chip to make an on-chip spectrometer with an operation bandwidth of 1.2 – 2.4 µm. Device A will function over the 1.2 – 1.7 µm wavelengths and Device B will cover 1.7 – 2.4 µm. The fabrication will be completed at the AIM Photonics foundry using an MPW run.

Since these devices operate at wavelengths far beyond the telecom bands, the design must start from the ground up, beginning with waveguide design. The challenge for broadband waveguide design is finding a single waveguide geometry that achieves adequate confinement and low bending loss for long wavelengths and still suppresses multimode propagation at smaller wavelengths. In order to use an MPW run for the fabrication, the waveguide thickness is fixed to the standard silicon thickness of 220 nm for SOI. With the thickness set, the only variable to explore is the waveguide width. Studying the mode profiles with an eigenmode expansion solver, initial simulations showed that device A must have waveguides narrower than O-Band standard widths and Device B must go wider than C-

Band waveguide norms. From that starting point, and parameter sweep was conducted to test potential waveguide widths (Fig. 8). The results show that Device A should have a waveguide width below 350 nm to support single mode operation over the wavelength range, but below 320 nm the waveguide does not support the fundamental TE mode above 1.5 µm. An analysis of bending loss for widths between these two bounds concluded that a width of 340 nm is the preferable width for Device A. Following the same methods for Device B, the waveguide width was set to 600 nm.

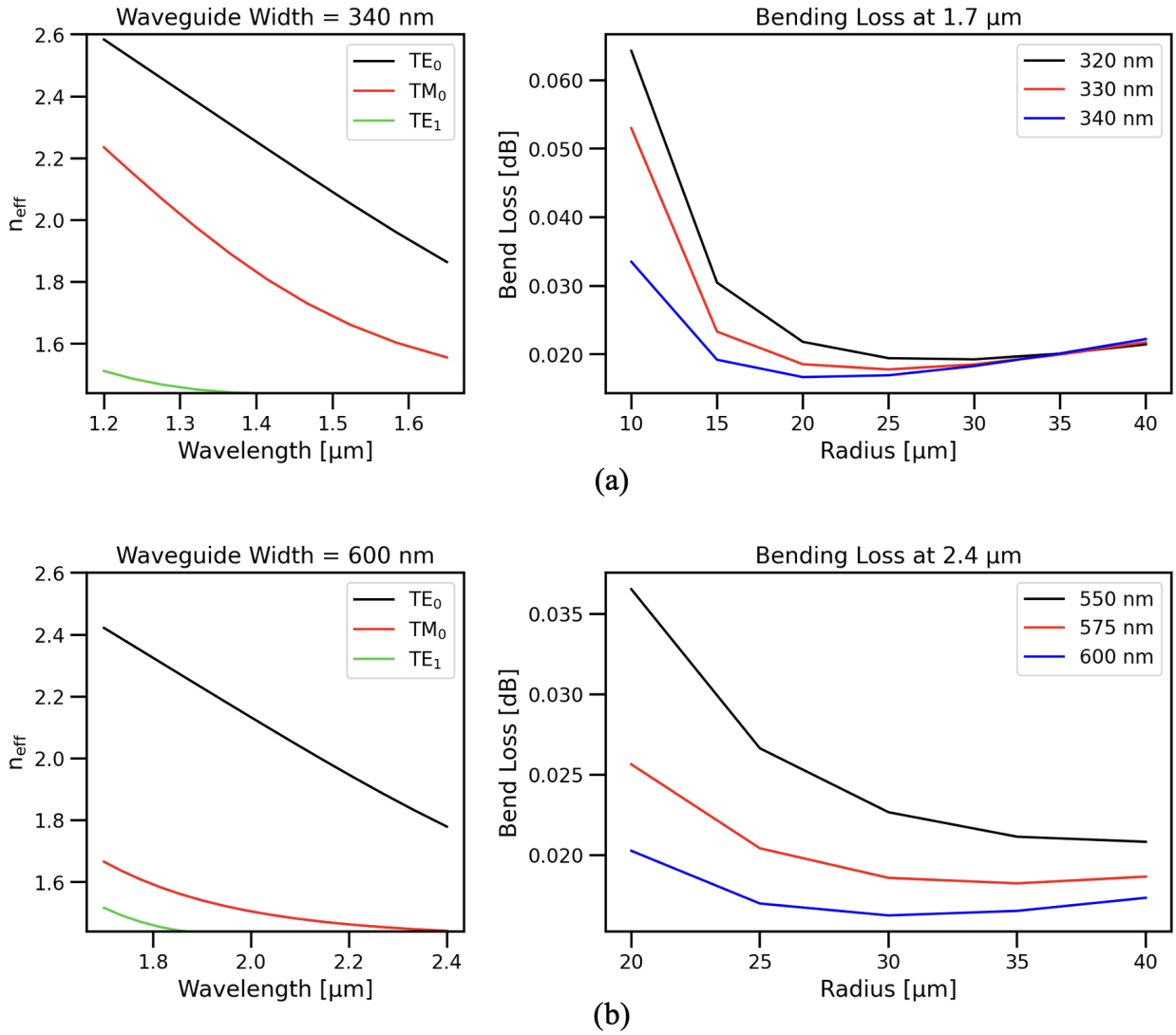

Figure 8: Waveguide simulation results for the ultra-broadband dFT chip. Single mode operation and bending loss were evaluated around (a) 320 - 350 nm for Device A and (b) 500 - 600 nm for Device B. The widths of 340 nm and 600 nm respectively were selected to minimize the bending loss for each dFT device while prioritizing single-mode operation.

Once the waveguide design was established, the next step was to develop the components necessary for an ultra-broadband dFT, specifically an adiabatic coupler that yields 3-dB power splitting over the operation range of each device. Since adiabatic couplers only ever excite one fundamental mode, they are inherently broadband given a sufficiently long coupling section.

The previous adiabatic coupler was designed for a waveguide width of 500 nm and a wavelength range of 1620 – 1750 nm. For this new spectrometer chip, a new adiabatic coupler was developed for each of the dFT devices. Creating the ultra-broadband adiabatic couplers was a matter of designing couplers compatible with each dFT's waveguide width while maintaining the adiabatic condition of the taper. For this, three-dimensional finite-difference time-domain (FDTD) simulations were used to optimize the waveguide asymmetry, that taper length, and the bend radius of the input-output s-bends. For Device A, the resulting design used an asymmetry of 120 nm and a taper length of 100 µm. For the longer wavelength device, a larger asymmetry of 250 nm and a longer taper length of 150 µm were required. For both coupler designs, it was determined that the s-bends must be at least 50 µm long for the desired waveguide separation in order to keep the bending radius large enough to limit back reflections in the coupling region. The broadband transmission of each coupler is provided in Figure 9. With further study of the adiabatic coupler design, the oscillations in the transmission spectra may be further minimized or eliminated completely.

One of the last factors of the design is the path length scaling. For these most recent designs, optimizing the path length scaling factor for regression quality and experimental logistics has been taken into consideration. By relating the resolution to the bandwidth and the number of spectral channels using the derived Rayleigh Criteria, it was determined that a smaller ΔL would make the device characterization less under-constrained and would therefore improve the quality of the regression used to solve for the characterization matrix. Furthermore, there is a limit to the wavelength steps that can be created experimentally which places an upper limit on the path length scaling factor. Following these two reasons, it was decided that a scaling factor of $\Delta L = 5$ µm would be suitable for both Device A and Device B.

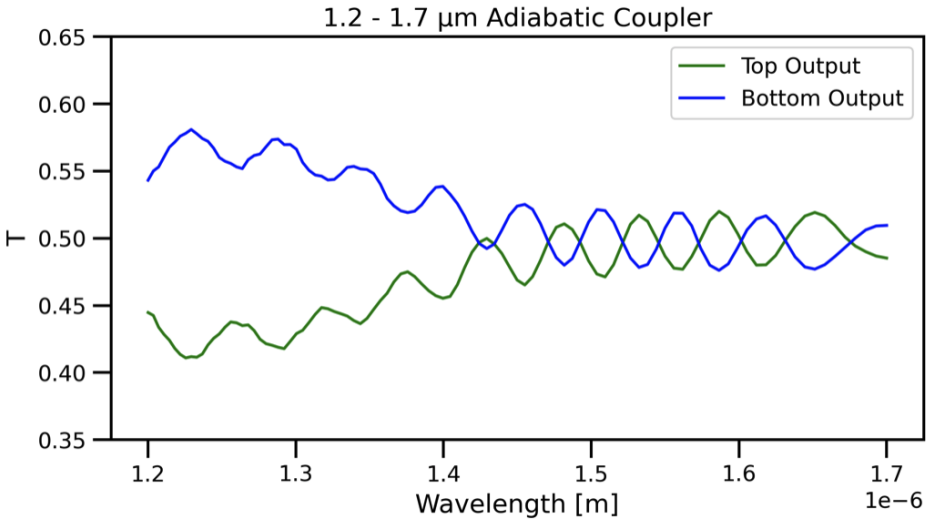

(a)

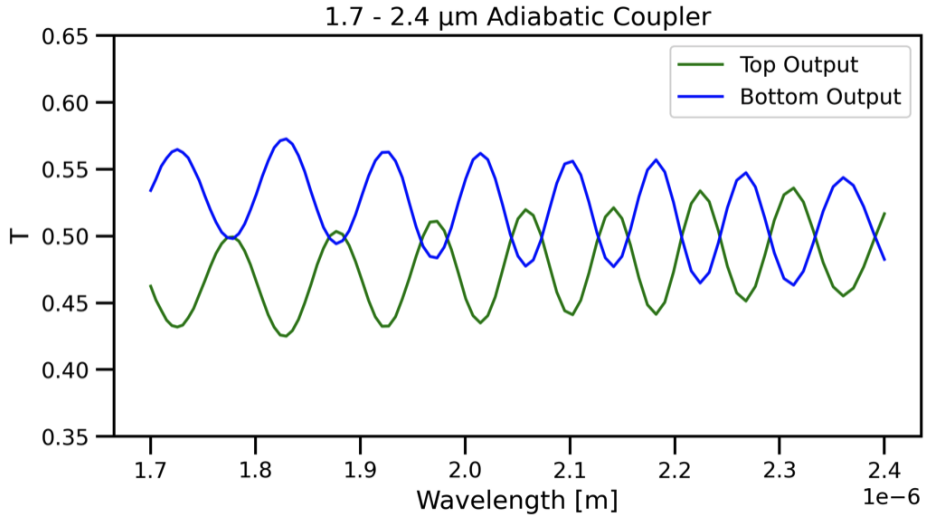

(b)

Figure 9: Broadband adiabatic coupler design. Simulations determined the power splitting for (b) the 1.2 - 1.7 µm coupler and (c) the 1.7 - 2.4 µm coupler (b). Each coupler provides approximately 3-dB power splitting across the broad operation range.

The final design consideration is the modulators that will be used for each device. After conferring with the foundry that will be fabricating the chips, we believe it will be possible to use the TO modulators from the foundry's PDK for the broadband devices. The O-Band TO modulator was used in Device A and the C-Band TO modulator was used for Device B. Before the design is finalized, further analysis is necessary to verify the viability of this option. While PDK components are the safer choice for consistency and reliability, using custom heaters may prove to be the better choice to meet the demands of these designs. Since the designs were drafted with the modular dFT package, this will be a simple edit to implement. Device fabrication will be completed later this year.

4 Conclusion

Chip-scale spectrometers are an evolving technology poised to revolutionize chemical sensing capabilities. While other efforts to miniaturize spectrometers have been held back by chip space limitation, our dFT spectrometer presents a solution in which resolution scales exponentially with the number of stages, drastically reducing the space required for a high-resolution device. The second generation of dFT spectrometers realize [**x**] resolution and half-octave broadband operation. The next sets of dFT devices are designed to achieve ultra-broadband performance, combining two spectrometers on a single chip for 1.2 - 2.4 µm operation. These designs were realized using a new modular scripting package that automates the design process. This programmatic approach created a reusable tool that dramatically reduces design and versioning time while maintaining the flexibility to customize the device.

With future designs, we aim to demonstrate the dFT's functionality in biomedical applications. On-chip spectrometers will be an advantageous addition to medical diagnoses tools like optical coherence tomography and can help make diagnostics less expensive and more accessible. Besides dFT designs and varied applications, another area of focus is the spectrum reconstruction method and the regression algorithm used to characterize devices. With this exploration, we will gain insight into how to optimize dFT design to improve the quality of regression used for finding the characterization matrix to best aid in the reconstruction of optical spectra.

In creating these devices, certain challenges have become apparent. One challenge our spectrometer platform faces is the implementation of the electronics required to power the dFT device. Miniaturizing the spectrometer must be paired with down-scaling the electronics to fully realize a portable, field-deployable spectrometer. Integrating the power electronics with the chip circuitry to create a stand-alone unit would be the ideal. Another challenge is the packaging currently available for photonic integrated circuits. Optoelectronic packaging requires maturation before high-volume, low-cost manufacturing of dFT devices is possible. As the field of integrated photonics continues to evolve, dFT spectrometers will be instrumental in furthering chemical sensing capabilities.

5 References

[1] P.T. Lin, V. Singh, J. Wang, H. Lin, J. Hu, K. Richardson, J.D. Musgraves, I. Luzinov, J. Hensley, L.C. Kimerling, and A. Agarwal. Si-CMOS compatible materials and devices for mid-IR microphotonics. *Opt. Mater. Express*, 3(9):1474, 2013.

[2] G. Roelkens, U. Dave, A. Gassenq, N. Hattasan, C. Hu, B. Kuyken, F. Leo, A. Malik, M. Muneeb, E. Ryckeboer, D. Sanchez, S. Uvin, R. Wang, Z. Hens, R. Baets, Y. Shimura, F. Gencarelli, B. Vincent, R. Loo, J. Van Campenhout, L. Cerutti, J. Rodriguez, E. Tournie, X. CHen, M. Nedeljkovic, G. Mashanovich, L. Shen, N. Healy, A. C. Peacock, X. Liu, R. Osgood, and W. M. J. Green. Silicon-based photonic integration beyond the telecommunication wavelength range. *J. Select. Topics Quantum Electron.*, 20:394–404, 2014.

[3] J. Bland-Hawthorn and P. Kern. Astrophotonics: a new era for astronomical instruments. *Opt. Express*, 17:1880–1884, 2009.

[4] J. G. Crowder, S. D. Smith, A. Vass, and J. Keddie. *Infrared Methods for Gas Detection*, pages 595–613. Springer London, London, 2006.

[5] P.W. Atkins. *Physical Chemistry*. Freeman, New York, 1978.

[6] John. McMurry. *Organic chemistry*. Thomson Brooks/Cole, Belmont, CA, 7th ed. edition, 2008.

[7] H. Pires, M. Baudisch, D. Sanchez, M. Hemmer, and J. Biegert. Ultrashort pulse generation in the mid-IR. *Progress in Quantum Electron.*, 43:1–30, 2015.

[8] R.G. Sellar and G.D. Boreman. Comparison of relative signal-to-noise ratios of different classes of imaging spectrometer. *Appl. Opt.*, 44:1614–1624, 2005.

[9] M. Harwit and N.J.A. Sloane. *Hadamard Transform Optics*. Academic Press, 1979.

[10] P. Hariharan. *Basics of Interferometry*. Academic Press, Burlington, MA, 2 edition, 2007.

[11] S. Zheng, H. Cai, Y. D. Gu, L. K. Chin, and A. Q. Liu. High-resolution on-chip spectrometer with a tunable micro-ring resonator filter. In *Conference on Lasers and Electro-Optics*, page AM1J.2. OSA, 2016.

[12] T. Chao, T.T. Lu, S.R. Davis, S.D. Rommel, G. Farca, B. Luey, A. Martin, and M.H. Anderson. Compact liquid crystal waveguide based fourier transform spectrometer for in-situ and remote gas and chemical sensing. 2008.

[13] J. Li, D. Lu, and Z. Qi. Miniature fourier transform spectrometer based on wavelength dependence of half-wave voltage of a LiNbO_3 waveguide interferometer. *Opt. Lett.*, 39(13):3923, 2014.

[14] M. C. M. M. Souza, A. Grieco, N. C. Frateschi, and Y. Fainman. Fourier transform spectrometer on silicon with thermo-optic non-linearity and dispersion correction. *Nat. Comm.*, 9(1):665, 2018.

[15] A. V. Velasco, P. Cheben, P. J. Bock, A. Delâge, J. H. Schmid, J. Lapointe, S. Janz, M. L. Calvo, D. Xu, M. Florjańczyk, and M. Vachon. High-resolution fourier-transform spectrometer chip with microphotonic silicon spiral waveguides. *Opt. Lett.*, 38(5):706, 2013.

[16] M. Nedeljkovic, A. V. Velasco, A. Z. Khokhar, A. Delage, P. Cheben, and G. Z. Mashanovich. Mid-infrared silicon-on-insulator fourier-transform spectrometer chip. *IEEE Photon. Technol. Lett.*, 28(4):528–531, 2016.

[17] A. Herrero-Bermello, A.V. Velasco, H. Podmore, P. Cheben, J.H. Schmid, S. Janz, M.L. Calvo, D. Xu, A. Scott, and P. Corredera. Temperature dependence mitigation in stationary fourier-transform on-chip spectrometers. *Opt. Lett.*, 42(11):2239, 2017.

[18] H. Podmore, A. Scott, P. Cheben, A. V. Velasco, J. H. Schmid, M. Vachon, and R. Lee. Demonstration of a compressive-sensing fourier-transform on-chip spectrometer. *Opt. Lett.*, 42:1440, 2017.

[19] H. Podmore, A. Scott, and R. Lee. On-chip compressed sensing fourier-transform visible spectrometer. *IEEE Photon. J.*, 10:6602010, 2018.

[20] D.M. Kita, H. Lin, A. Agarwal, K. Richardson, I. Luzinov, T. Gu, and J. Hu. On-chip infrared spectroscopic sensing: Redefining the benefits of scaling. *IEEE J. Select. Topics Quantum Electron.*, 23(2):340–349, 2017.

[21] D.M. Kita, B. Miranda, D. Favela, D. Bono, J. Michon, H. Lin, T. Gu, and J. Hu. High-performance and scalalble on-chip digital fourier transform spectroscopy. *Nat. Comm.*, 9:4405, 2018.

[22] D.M. Kita, B. Miranda, D. Favela, D. Bono, J. Michon, H. Lin, T. Gu, and J. Hu. High-resolution on-chip digital fourier transform spectroscopy. In *Conference on Lasers and Electro-Optics*, page SF1A.1. OSA.

[23] Liang Cao, Ali Elshaari, Abdelsalam Aboketaf, and Stefan Preble. Adiabatic couplers in SOI waveguides. In *Conference on Lasers and Electro-Optics 2010 (2010), paper CThAA2*, page CThAA2. Optica Publishing Group, May 2010.

[24] Luhua Xu, Yun Wang, David Patel, Eslam El-Fiky, Zhenping Xing, Rui Li, Md Ghulam Saber, Maxime Jacques, and David V. Plant. Polarization Independent Adiabatic 3-dB Coupler for Silicon-on-Insulator. In *Conference on Lasers and Electro-Optics (2017), paper SF1I.5*, page SF1I.5. Optica Publishing Group, May 2017.

[25] Heba Tamazin, Eslam El-Fiky, Yun Wang, Yannick D'Mello, David Patel, Amar Kumar, and David V. Plant. Ultra-broadband Compact Adiabatic Coupler in Silicon-on-Insulator for Joint Operation in the C- and O-Bands. In *Conference on Lasers and*

Electro-Optics (2018), paper STh4B.4, page STh4B.4. Optica Publishing Group, May 2018.

[26] E.D. Palik. *Handbook of Optical Constants of Solids*, volume 2. Academic Press, Boston, Massachusetts, 1998.

[27] R. Soref. Silicon photonics technology: past, present, and future. page 19. SPIE, 2005.